View metadata, citation and similar papers at core.ac.uk
brought to you by CORE
provided by RERO DOC Digital Library

Exp Fluids (2012) 52:1349–1360
DOI 10.1007/s00348-011-1256-2

RESEARCH ARTICLE

3D-PTV measurements in a plane Couette flow

Dominik Krug · Beat Lüthi · Hansjörg Seybold · Markus Holzner · Arkady Tsinober

Received: 8 July 2011 / Revised: 13 December 2011 / Accepted: 19 December 2011 / Published online: 7 January 2012
© Springer-Verlag 2012

Abstract Genuine plane Couette flow is hard to realize experimentally, and no applications of modern spatially resolving measurement techniques have been reported for this flow so far. In order to resolve this shortcoming, we designed and built a new experimental facility and present our first results here. Our setup enables us to access the flow via 3D particle tracking velocimetry and therefore to obtain truly three-dimensional flow fields for the first time experimentally in plane Couette flow. Results are analyzed in terms of basic flow properties, and a clear distinction of flow regimes (laminar for $Re < 320$, transitional for $320 < Re < 400$, and turbulent when $Re > 400$) could be made. Comparison with DNS data shows good agreement in the turbulent regime and builds trust in our data. Furthermore, vortical coherent structures are studied in detail with the additional help of kalliroscope imaging, and the typical vortex spacing is determined to be roughly one gap width. As a noteworthy result, we find that the onset of the turbulent regime coincides with the range of Reynolds numbers at which a distance of 100 wall units is comparable to the gap width.

D. Krug (✉) · B. Lüthi
Institute of Environmental Engineering, ETH Zurich,
8093 Zurich, Switzerland
e-mail: krug@ifu.baug.ethz.ch

H. Seybold
Department of Earth, Atmospheric, and Planetary Sciences,
Massachusetts Institute of Technology, Cambridge,
MA 02139-4307, USA

M. Holzner
Max Planck Institute for Dynamics and Self-Organization,
37073 Goettingen, Germany

A. Tsinober
The Iby and Aladar Fleischman Faculty of Engineering,
Tel Aviv University, 69978 Ramat Aviv, Israel

1 Introduction

Despite the relative simplicity of its base flow, the linearly stable plane Couette flow (pCf) still poses a very hard challenge for the turbulence community in terms of understanding its transition and turbulence dynamics. In recent times, research has focussed mostly on the numerical side and has produced fruitful results: Nagata (1990) was the first to discover exact equilibria and traveling waves (Nagata 1997) in pCf. Among others (for a recent review, see Gibson et al. 2009), Waleffe (2003) contributed *exact coherent structures* by constructing them along the lines of his self-sustaining process in shear flows (Waleffe 1997). These results are stepping stones toward a dynamical systems theory, where the ultimate goal is to model turbulent dynamics in the transitional regime through the dynamics and connections of exact invariant solutions (Gibson et al. 2008, 2009). However, most of the exact solutions were obtained on relatively small computational domains that are barely large enough for turbulence to be sustained. In fact, these numerical studies focus mostly on temporal evolutions and are typically not able to capture the growth of localized turbulent regions or the coexistence of turbulent and non-turbulent patterns observed in real systems. Due to relaxed requirements on the resolution and increasing computer power, it has recently become possible to overcome this issue and to perform simulations on domains of $\mathcal{O}(100)$ times the minimal size to sustain turbulence. Philip and Manneville (2011) report an investigation on the minimum domain size to obtain spatiotemporal dynamics while related late

work (Rolland and Manneville 2011; Duguet et al. 2010; Tuckerman and Barkley 2011) scrutinizes the formation and properties of turbulent-laminar banded patterns. Schneider et al. (2010) extended the search for *edge states*, i.e., flow patterns that lie on the boundary between turbulent and laminar regimes in state space, to larger domains.

The earliest account of the struggle an experimentalist may face trying to set up genuine pCf was published by Reichardt (1959). Probably owing to these practical difficulties, experimental studies have remained rather scarce throughout. Aydin and Leutheusser (1991) give a short summary of the early work that focussed, just like the later investigations by Bech et al. (1995) and Malerud et al. (1995), mostly on fully turbulent states with Re of $\mathcal{O}(1000)$. Tillmark and Alfredsson (1992) pioneered the detailed exploration of the transitional regime in pCf by triggering turbulent spots, an approach that was subsequently followed by Daviaud et al. (1992) and Hegseth (1996). A different kind of perturbation was introduced by Dauchot and Daviaud (1995) who used a wire spanned in the neutral velocity plane along the spanwise direction to slightly deform the velocity profile. Their analysis was later on extended experimentally (Bottin et al. 1997; Bottin and Chaté 1998; Antar et al. 2003) and numerically (Barkley and Tuckerman 1999). Bottin and Chaté (1998) combined the analysis of turbulent spots with an investigation of the reverse transition by so-called quench experiments in order to perform a statistical analysis of turbulence lifetimes. Some of the latest experimental results are due to Prigent et al. (2003) who observed oblique turbulent stripes, closely related to the "spiral" or "barbers's pole" turbulence in Taylor Couette flow when reducing Re starting from a turbulent state. This pattern is the subject of a numerical analysis by Barkley and Tuckerman (2007), while simulations by Schmiegel and Eckhardt (2000) suggest that turbulence might persist down to $Re \approx 280$ if the Reynolds number is reduced carefully. All the experiments reported in the literature so far utilize flow visualizations or point measurements by Laser Doppler velocimetry or hot wire anemometry. To bridge the gap to modern spatially and temporally resolved techniques, we designed a flow facility that is suitable for three-dimensional particle tracking velocimetry (3D-PTV). Specifically, this means using a considerably larger gap width (3 cm instead of few millimeters in most other recent realizations) to obtain proper optical access making it somewhat more costly to reach large aspect ratios. Our newly build setup enables us to present for the first time truly 3D velocity fields along with quantities such as the turbulent kinetic energy and the Reynolds shear stress tensor. We will present these results together with a comparison to direct numerical simulations.

2 Method

A sketch of the plane Couette setup is shown in Fig. 1. Movement is generated by a looped conveyor belt that is driven by an electric motor attached to the top roller. Two pairs of smaller cylinders provide additional guidance and can be used to fine tune the position of the belt. Severe buckling problems with the relatively large belt prohibited the use of transparent material. Ultimately, we therefore had to deviate from our original plan to measure in between the up- and downwards moving sections of the belt. The pCf in our apparatus now evolves between the moving belt, consisting of a fairly solid intransparent conveyor belt, and a glass plate located parallel to it. In contrast to most realizations of pCf reported in the more recent literature (e.g., Bottin and Chaté 1998; Tillmark and Alfredsson 1992), this configuration results in a mean advection of half the belt speed, necessitating a careful handling of the backflow outside the domain. For this purpose, turning vanes are installed to guide the flow around the corners; additionally, the inflow is becalmed by honeycombs before (length:

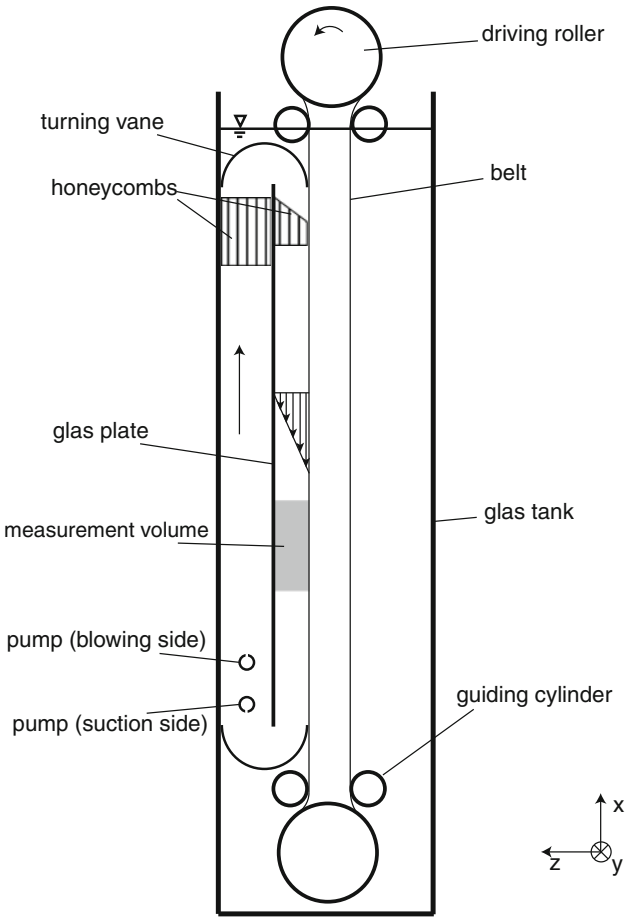

Fig. 1 Schematic of the experimental setup

10 cm, tube diameter: 5 mm) and after (tapered at an angle of 34° to enhance profile development, length: 5 cm on the longer side, tube diameter: 3.5 mm) the upper turning point. The entire setup is placed in a glass container and submerged into deionized water, the working fluid in the experiment. The coordinate system (see Fig. 1) used throughout this study is oriented in a way that the x-axis runs in the streamwise direction positive in the opposite direction of the belt velocity. The y-axis denotes the spanwise direction, and the z-axis runs normal to the walls starting with zero at the belt. Velocity components in the three directions (x, y, and z) are denoted by u, v, and w or abbreviated by u_i, where appropriate. The dimensions of the flow domain are $L_x = L_y = 1.6$ m and $L_z = d = 3.12$ cm. This results in an aspect ratio of $\Gamma_x = \Gamma_y = L_{x/y}/(d/2) = 106.6$. In order to minimize boundary effects, the flow is contained by glass walls positioned at both sides along the edge of the belt. The gap between the glass and the moving belt is sealed by brush seals.

A pump is used to compensate pressure losses in the return flow. The intake and the outflow of the pump are evenly distributed over the entire width of the flow by using segmented pipes featuring an array of small holes. The correct pump setting was obtained by evaluating experimentally obtained velocity profiles. A straightforward measure to judge whether the pump setting is correct that is applicable in the laminar as well as the turbulent case is to check whether the streamwise velocity at half the gap width equals half the belt speed. By iteratively adjusting the pump setting for a given Reynolds number, we typically managed to keep $u|_{z=d/2} - u_{\text{belt}}/2$ below 4% of u_{belt}. Another criterion of the quality of the base flow is to check for the symmetry of the profiles. In order to quantify the symmetry, we define the normalized integral $S = \int_0^d \Delta u(z)\mathrm{d}z/(u_{\text{belt}}d)$, where $\Delta u(z)$ is the difference between the measured velocity and the linear profile at any given z-position. In case of a perfectly symmetric profile, S goes to zero and—unlike the skewness—does not diverge for the profiles in the laminar regime. The values we obtain for S (see Fig. 3) are usually below 4% of $u_{\text{belt}}d$.

The Reynolds number in a setup like this is commonly defined using half the gap width, d, and half the belt speed, u_{belt}, such that $Re = u_{\text{belt}}\, d/(4\nu)$, with ν being the kinematic viscosity. The speed u_{belt} at a given motor setting was obtained from measurements of the time between the passage of two marks of known distance on the belt and could thereby be determined to within $\Delta u_{\text{belt}} = 0.0005$ m/s. The gap was measured within an estimated error of $\Delta d = 0.6$ mm or 2% of its actual value. Lastly, ν was obtained by taking temperature measurements and interpolating them to literature values of ν. The accuracy of this procedure is estimated to be within 1% of the actual value.

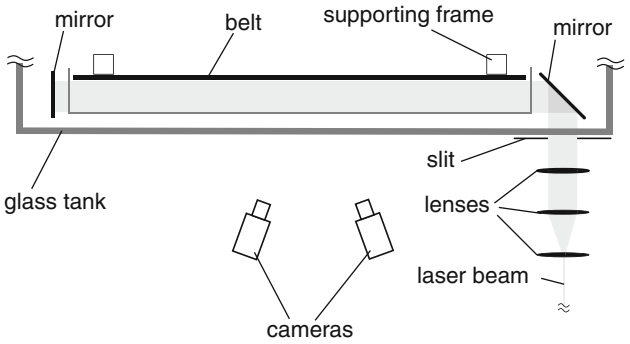

Fig. 2 Illustration of the lightpath and camera setup (two out of four cameras shown)

Thus, the resulting maximum relative error in the determination of Re is of the order of 3%.

As mentioned earlier and depicted in Fig. 2, the flow is accessible for flow visualization via 3D particle tracking velocimetry (PTV). This image-based measurement technique makes use of the stereoscopic principle to reconstruct particle positions in space (Racca and Dewey 1988; Malik et al. 1993; Maas et al. 1993; Virant and Dracos 1997). In theory, it is sufficient to use images taken from at least two different positions. Still, we record the flow field using four cameras, which turned out to be effective in reducing ambiguities in the particle detection while keeping cost and space requirements limited. By linking particle positions over several subsequent frames using a tracking algorithm (see e.g., Ouellette et al. 2006 for details), their trajectories and hence the three-dimensional velocities can be determined. For our study, we use a code that was developed in house and that is also publicly available from http://ptv.origo.ethz.ch/. The measurement volume of the approximate size of 17 × 16 × 3 cm^3 was illuminated by a 15 W Ar-Ion Laser using an array of lenses and mirrors. The streamwise position of the measurement volume can be varied; if not mentioned otherwise, it was located 75 cm ($\sim 25d$) downstream of the tapered honeycomb. The flow is seeded with neutrally bouyant polyamid particles with a mean diameter of 100 μm (trade name: Vestosint 1101, manufactured by Evonik Industries, Germany). Typical seeding densities were between 2.4 and 3.6 particles/cm^3. Images are recorded by all four cameras simultaneously at a resolution of 1,280 × 1,024 pixel and a frame rate of 50 Hz. The necessary calibration of the camera setup was achieved in two steps. At first, a flat calibration target glued onto the belt was used to obtain a raw orientation data set. This then served as the starting point for a dynamic calibration using the so-called shaking algorithm. Instead of using known locations of target points, this algorithm fine-tunes the calibration by minimizing the offset of epipolar lines corresponding to the same particle in object space. To

Table 1 Noise level of turbulence intensity, I, and rms velocity fluctuations as obtained at $Re = 180$

Component	I (%)	rms (10^{-4} m/s)
x	2.0	4.43
y	1.34	2.97
z	3.16	7.01
All	2.31	5.12

gauge the overall quality of the experimental setup comprising the accuracy of the calibration and velocity fluctuations due to inflow perturbations, turbulence intensity levels, I, and rms-fluctuations are reported for all three velocity components in a nominally laminar flow at $Re = 180$ in Table 1. These values can be regarded as an upper bound on the measurement error.

For each Reynolds number reported, we reconstruct the trajectories of the PTV tracer particles using 100 successive frames. This corresponds to 2 s or 1.4–4 time units d/u_{belt} at $Re = 180$ to $Re = 500$, respectively. Profiles of flow quantities as a function of the z-component were calculated by averaging in time as well as over slices of 0.5 mm thickness in wall-normal direction spanning over the entire measurement domain in x and y. The average is depicted by $\langle\cdot\rangle$. Figure 3 shows examples of resulting streamwise velocity profiles in the laminar (Fig. 3a) and the turbulent regime (Fig. 3b).

In order to gain insight into larger scale structures present in the flow, the PTV measurements were augmented by investigations using a seeding of kalliroscope particles. These flake-like particles align with the shear in the flow (Matisse and Gorman 1984). They were illuminated by a thin laser sheet and images of a domain of approximately 0.5×0.5 m^2 were recorded.

Further, we compared our experimental results with numerical simulations. To this end, we solved the time-dependent Navier Stokes equations subject to stream- and spanwise periodic boundary conditions on a box of size $[L_x^{\text{DNS}}, L_y^{\text{DNS}}, L_z^{\text{DNS}}] = [15, 15, 2]$ using the spectral code Channelflow (Gibson 2009), which uses Fourier series with periodic boundary conditions in stream- and spanwise directions and Chebychev polynomials for the wall–wall discretization (Canuto et al. 1998; Gibson 2009). The time integration was performed using a third-order Adams-Bashford Backward-Differentiation scheme with adaptive time stepping (Peyret 2002; Gibson 2009). Starting from a field randomly perturbed in Fourier space, the integration was carried out over 10,000 time units d/u_{belt}. The first 500 time units of each run were discarded for initialization in order to obtain an undisturbed fully developed turbulent field. Unless mentioned otherwise, a spectral resolution of $[96 \times 192 \times 49]$ in x, y, and z-direction was used.

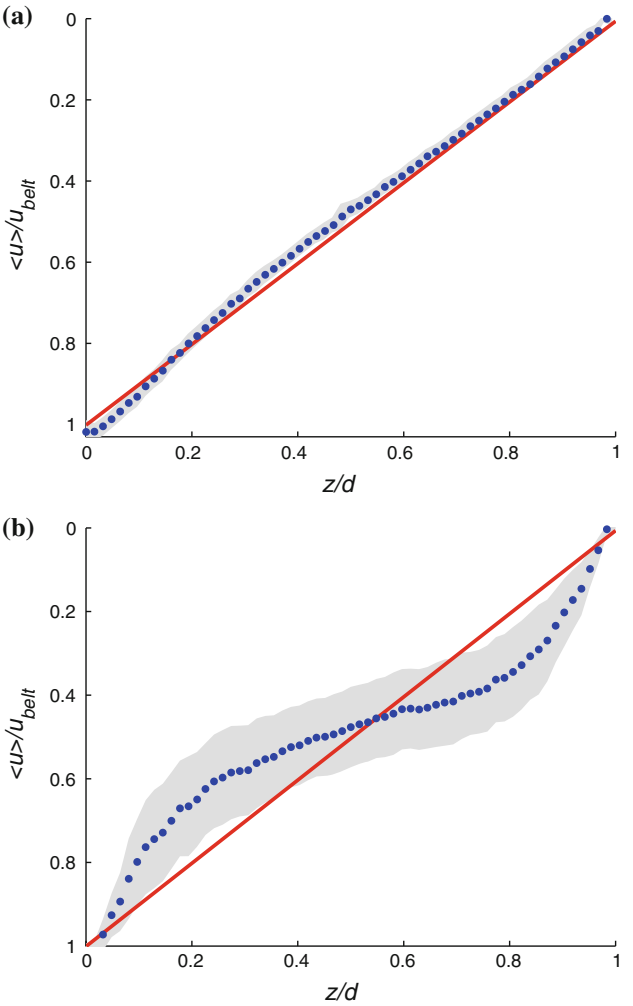

Fig. 3 Velocity profiles of the streamwise component (*blue symbols*) including rms-fluctuations (*shaded gray area*). The *thick red line* represents the linear profile. **a** $Re = 180$, laminar, **b** $Re = 450$, turbulent

Averages of flow quantities were taken in the same way as in the experiment.

3 Experimental results

The main features characterizing the velocity profiles shown in Fig. 3 are their global shape represented by the mean value of streamwise velocity and its rms-fluctuations indicated by the shaded gray area. In general, there are two factors influencing the observed shape of the velocity profiles at the measurement location with opposing effects: in the laminar regime, the flow relaxes from the more plug-like inflow distribution and constantly reduces the deviation from the linear profile as the fluid travels downstream. At the same time, advective transport of x-momentum due to velocity fluctuations reduces the velocity gradient in the

core of the domain as the flow becomes turbulent, resulting in larger deviations from the linear profile or, as one might say, a stronger 's-shape'. In order to quantify the shape of the profiles and to assess the impact of the two effects as a function of the Reynolds number, a sine function of the form $f(z) = A\sin\left(\frac{2\pi}{d}z\right)$ was fitted to the residual difference between measured velocities and the linear profile as shown in the inset in Fig. 4. The main plot presents amplitudes, A, as a function of Re at two different downstream positions. The results at the original measurement position show a roughly linear increase of A until it steeply increases to about twice its original value going from $Re = 400$ to $Re = 425$. The comparison with values

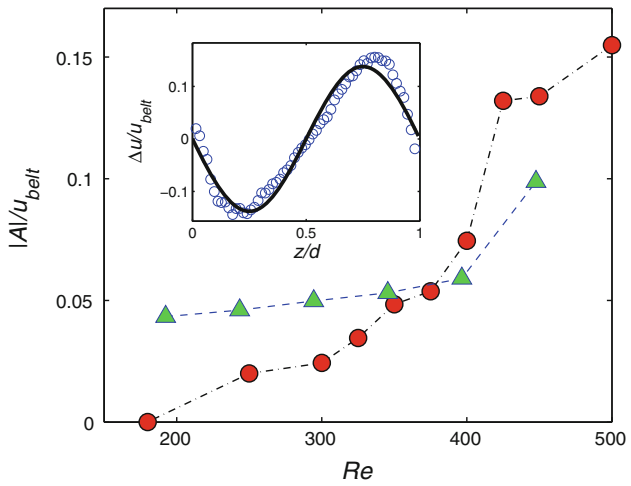

Fig. 4 Amplitude, A at two different locations: regular measurement position $\sim 25d$ downstream of the inflow (*red circles*) and a volume located 30 cm ($\sim 10d$) upstream of this position (*green triangles*); *Inset*: exemplary difference between measured and linear velocity profile (*blue circles*) and fit of the form $f(z) = A\sin\left(\frac{2\pi}{d}z\right)$ (*solid line*) at $Re = 450$

obtained 30 cm ($\sim 10d$) upstream of this position clearly marks the regime of laminar relaxation up to $Re \approx 375$ and turbulent mixing increasing the "s-shape" from there onwards. This implies that only above $Re = 375$ inflow perturbations are strong enough to trigger turbulence that will persist long enough to reach the downstream position.

The standard deviation of the velocity signal represented by the shaded gray areas in Fig. 3 can—apart from a certain noise level due to measurement inaccuracies—be attributed to velocity fluctuations that are commonly characterized by the turbulent kinetic energy (TKE), defined as:

$$E^t = \frac{1}{2}\left(\langle (u')^2\rangle + \langle (v')^2\rangle + \langle (w')^2\rangle\right), \tag{1}$$

where fluctuations $u_i' = u_i - \langle u_i\rangle$ are defined with respect to a mean taken over thin slices parallel to the xy-plane. Note that $\langle\cdot\rangle$ denotes an average taken over the entire measurement domain and time when applied to kinetic energies (yielding a scalar) and only a mean taken over thin slices parallel to the xy-plane, otherwise (yielding profiles as a function of z). Figure 5 presents values of TKE as a function of Re. In addition to E^t (Fig. 5a), the figure also displays the single components $\langle (u')^2\rangle$, $\langle (v')^2\rangle$, and $\langle (w')^2\rangle$ (Fig. 5b). It will later be shown that the scatter in these figures stems from slow temporal fluctuations of the signal. These fluctuations were accounted for by taking several measurements at each Reynolds number well spaced out in time. Clearly, TKE should be zero in the laminar regime. However, as discussed earlier, there is a certain noise level attributed to inaccuracies in the measurement process and to imperfections of the flow facility, mainly the inflow conditions. The fact that the noise level in dimensional numbers (inset in Fig. 5a) is constant within statistical fluctuations over the range of $180 < Re < 300$ gives us

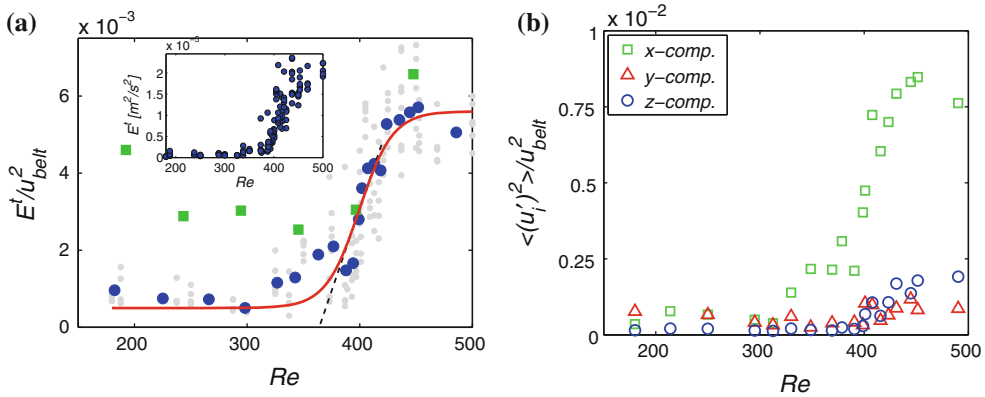

Fig. 5 **a** Turbulent kinetic energy (*blue circles*); *data points* represent the average of 7 measurements, original data are indicated by *light gray dots*. The *inset* shows the same data in dimensional units. *Green squares* indicate single measurements taken at a position 30 cm ($\sim 10d$) upstream. *Red line* represents the fit according to Eq. 2. **b** Decomposition of TKE (*blue circles* in **a**) into single components $\langle (u_i')^2\rangle$

confidence that the values presented in Table 1 are taken far enough downstream to be unaffected by decaying inflow perturbations. Nevertheless, upstream measurements (Fig. 5a, green squares) indicate that considerable fluctuations originate from the inflow and, dependent on the Reynolds number, die out or amplify as the flow travels through the domain. The increase in TKE happening on the broad range of approximately $Re = 320$ to $Re = 400$ marks the gradual transition from laminar flow to turbulence. In order to estimate a more precise value of a transitional Reynolds number, Re_{tr}, at which transition starts in this experiment, a function of the form

$$E^t(Re)/u_{\text{belt}}^2 = NL + \frac{a}{1 + e^{-b(Re+c)}} \tag{2}$$

was fit to the data. Defining Re_{tr} as the Reynolds number at which the tangent on the inflection point of the fit intersects the normalized noise level, $NL = 0.5 \times 10^{-3}$, yields $Re_{tr} = 370$. It is also instructive to follow the behavior of the single components of the TKE shown in Fig. 5b: while all three components appear equally strong as long as the flow remains laminar, $\langle (u')^2 \rangle$ is dominant after the transition; in the range of approximately $300 < Re < 400$, it is even solely responsible for the slight increase in overall TKE. As outlined in Tennekes and Lumley (1994), the dominance of $\langle (u')^2 \rangle$ may be explained by the fact that turbulent production in the i-th component

$$P_i = -\langle u_i' u_j' \rangle \frac{\partial \langle u_i \rangle}{\partial x_j} \text{ (no sum over } i) \tag{3}$$

relies on velocity gradients in the mean field. Even when the averaging was carried out more carefully by resolving the mean velocity field in all three directions instead of just the z-component, only the production term associated with $\frac{\partial \langle u \rangle}{\partial z}$ proved to be significant. Thus, only the x-component can receive energy directly from the mean flow, whereas the other components are solely fed by intercomponent transfer of energy through the pressure-strain terms, $\left\langle p' \frac{\partial u_i'}{\partial x_i} \right\rangle$ (no sum over i). It remains unclear why exactly this transfer is obviously not strong enough to render at least the unrestricted spanwise component approximately equal to $\langle (u')^2 \rangle$ as it is observed in other turbulent flows.

The $\langle u'w' \rangle$-component of the Reynolds stress tensor is responsible for the transport of x-momentum in the z-direction and therefore closely related to the evolution of the shape of the velocity profiles shown in Fig. 4. Plots of $\langle u'w' \rangle$ as a function of z are presented in Fig. 6. As a consequence of the particle tracking procedure, there are poorer statistics and slightly higher inaccuracies deeper in the domain. Due to the symmetry of the flow, the region closer to the belt, i.e., $z < 0.5d$, can be discarded without loss of information. As expected, the correlations of the

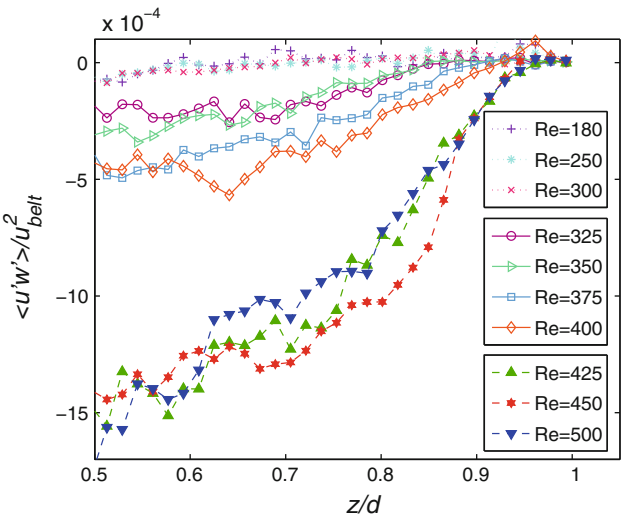

Fig. 6 Wall-normal profiles of the $\langle u'w' \rangle$-component of the Reynolds stress tensor. A distinction is made between a laminar (*dotted lines*), a transitional (*solid lines*) and a turbulent regime (*dashed lines*)

fluctuations exhibit a maximum in the middle of the channel and reduce to zero close to the wall. For Reynolds numbers up to 300 (dotted lines), $\langle u'w' \rangle$ remains essentially zero throughout the entire channel proving that the small fluctuations in this regime (that reflected themselves in a nonzero TKE for this nominally laminar flow, see Fig. 5) are in fact uncorrelated noise. The laminar regime is followed by what may be termed "transitional regime" comprising the lines for $Re = 325$ up to $Re = 400$ (solid lines). Here, the Reynolds stress attains clearly a nonzero value in the middle of the channel and increases slightly as a function of Re. A very pronounced increase to roughly 3 times the original value marking the beginning of the turbulent regime is observed between the curves for $Re = 400$ and $Re = 425$ (dashed lines). Judging from the experimental results, there seems to be no clear dependence of $\langle u'w' \rangle$ on Re within the turbulent regime.

Generally, we did not encounter any signs of spatio-temporal intermittency. Therefore, even in the transitional regime, the results presented do not represent averages of turbulent and non-turbulent regions but characterize a more or less homogenous flow state.

An observation of the flow by naked eye reveals that velocity fluctuations in the transitional and turbulent regime are not completely random but possess also organized patterns. In order to give an insight into these coherent structures, Fig. 7 presents plots of the y-z-view of the field of trajectories along with isosurfaces at which the flow speed equals half the respective belt speed. The isosurfaces were obtained by interpolating Lagrangian data over 100 frames (~2 s) onto a regular Eulerian grid. At $Re = 325$, there is no visible pattern in the trajectories and the isosurface remains flat. The situation changes slightly at

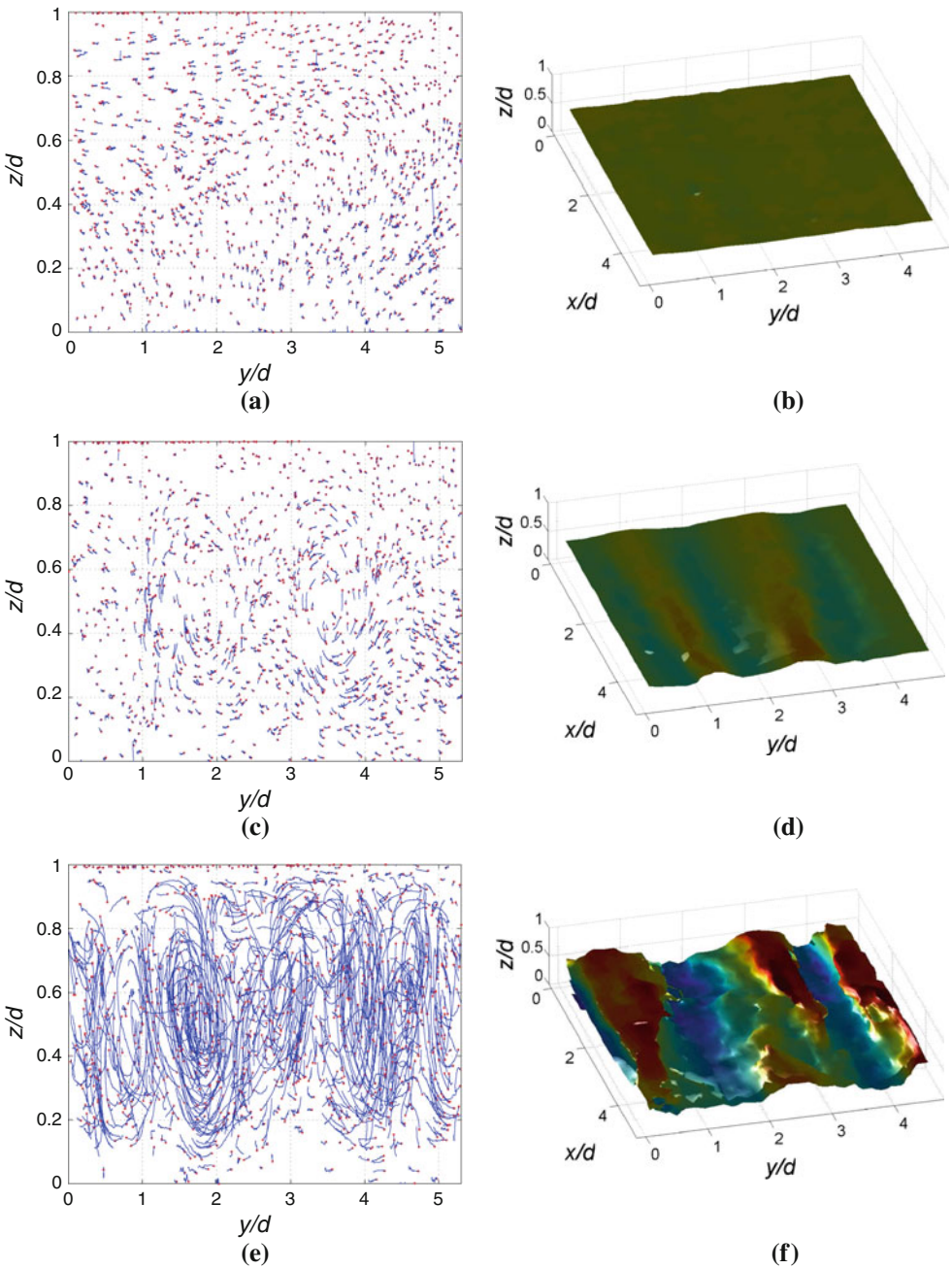

Fig. 7 *y*-*z*-view of trajectories of a minimum length of 35 frames with *red circles* indicating the start position (*left column*) and an isosurface of streamwise velocity at which $u = 0.5\ u_{\mathrm{belt}}$ obtained by interpolating the data on a regular grid (*right column*) with *color* coding of the *z*-position. **a** $Re = 325$, **b** $Re = 325$, **c** $Re = 350$, **d** $Re = 350$, **e** $Re = 500$, **f** $Re = 500$

$Re = 350$ were trajectories indicate the existence of weak organized streamwise vortices and the isosurface accordingly features wavy structures, resulting from the transport of *x*-momentum in the wall-normal direction. Finally, in the turbulent case at $Re = 500$, the flow field clearly features several vortical structures while the isosurface has a much higher amplitude in *z*-direction. The patterns are no longer uniform in *x* indicating a shorter streamwise extent of the structures at higher Reynolds numbers. From the data, the size of the rollers could be determined to approximately 3–5 cm ($\sim$1–1.5*d*) in *y* direction and filling almost the entire gap in the direction normal to the walls.

The trace of the vortical structures could also be identified clearly in the images with kalliroscope seeding (see Fig. 8 for sample pictures at different *Re*). These recordings allow for a more accurate quantification of the vortex spacing when analyzed in terms of the power spectral density of their light intensity distribution. Figure 9 compares the premultiplied normalized power spectral density (PSD), $k\mathrm{PSD}/I_0^2$ in the streamwise to those in the cross-stream direction for four different Reynolds numbers. The spectra are plotted as a function of the wavelength, λ, that is related to the wavenumber, k, by $\lambda = 2\pi/k$ and I_0 is the mean gray value intensity of the respective image. By

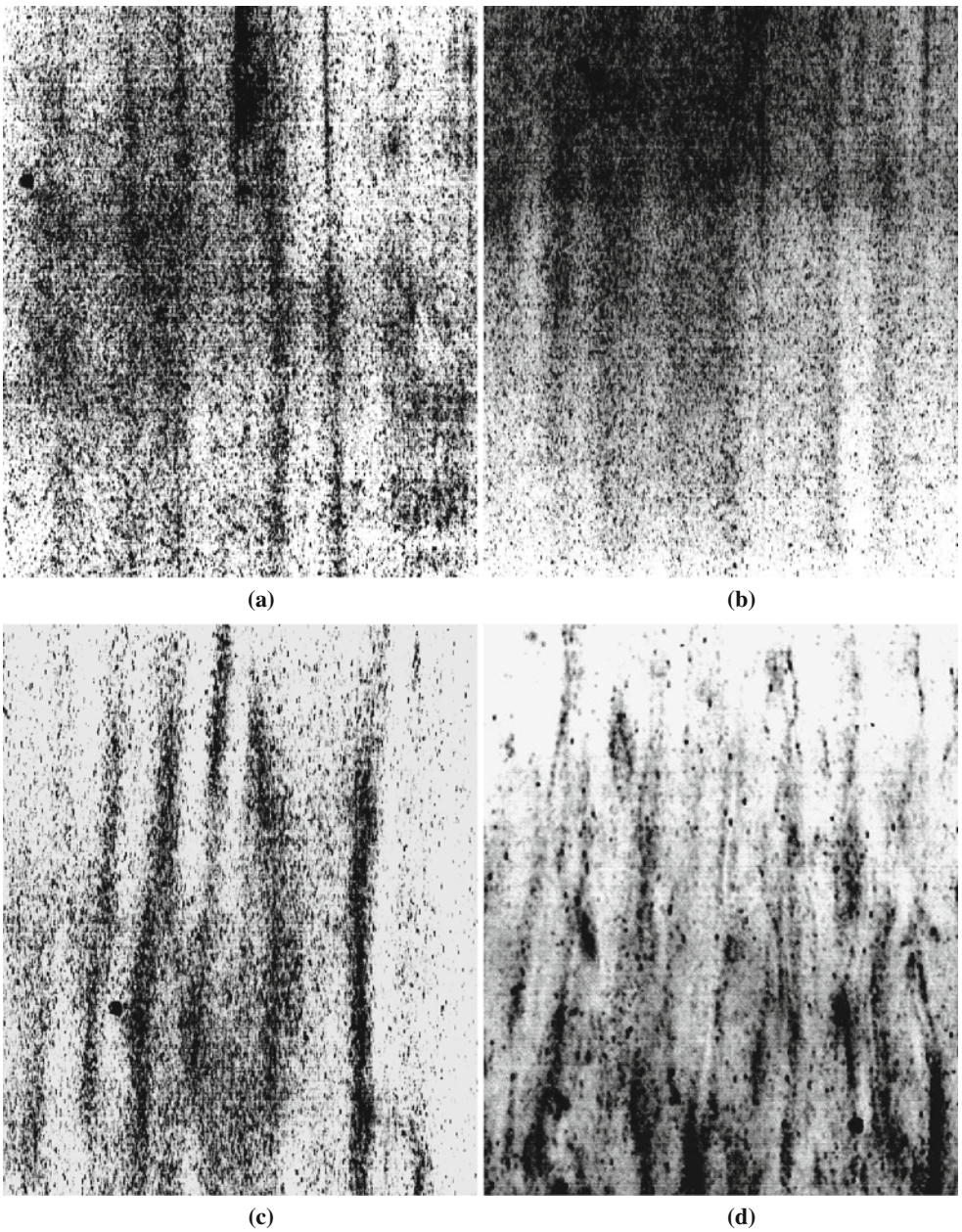

Fig. 8 Cutout of a sample images with kalliroscope seeding at different Reynolds numbers, *grayscale* inverted. The shown domain is about 21 cm wide and 30 cm long, the flow direction is from *top* to *bottom*. **a** $Re = 290$, **b** $Re = 340$, **c** $Re = 390$, **d** $Re = 440$

presenting the data in this way, patterns in the cross-stream direction stand out against the mostly featureless streamwise spectrum that serves as a characterization of the background distribution of light intensity in the images. At the lowest Reynolds number of 290, there is only little difference between the two directions but two weak peaks are already visible around $\lambda = d$ and the higher harmonic at $\lambda = 2d$. At $Re = 340$, the peaks in the transverse direction are more distinct while remaining at the same wavelengths. This signal appears strongest at $Re = 390$. However, in the turbulent regime ($Re > 400$) where Fig. 7 shows the strongest structures, the signal is again slightly weaker. While this may seem contradictory at first, it is well explained by the fact that in the turbulent regime, the vortices—due to a stronger interaction among themselves and their breakdown—are of much shorter streamwise extend as can be verified from Figs. 7f and 8d. Thus, the first peak at $\lambda = d$ is slightly lowered and its higher harmonic even falls below the signal in the streamwise direction.

Further, a noteworthy observation can be made by comparing the spacing of the streamwise coherent

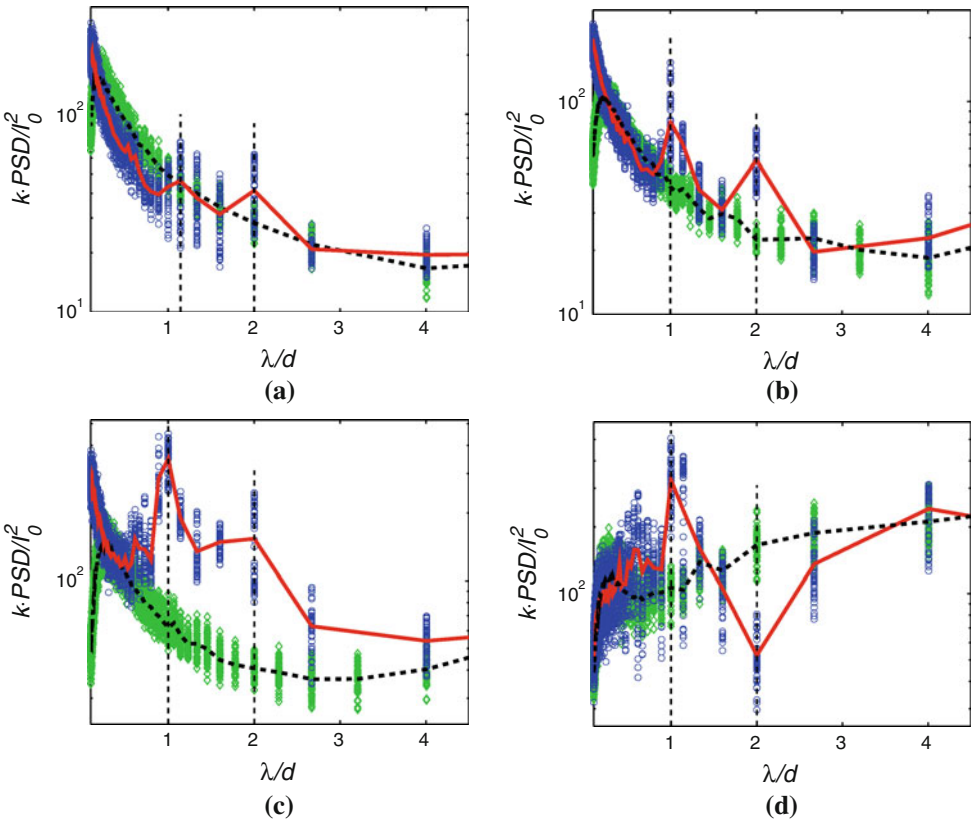

Fig. 9 Premultiplied power spectral density (PSD) of the light intensity distribution of the flow seeded with kalliroscope particles in streamwise (*green diamonds*) and spanwise (*blue circles*) direction The PSDs are premultiplied with the wavenumber, k, normalized with the average light intensity, I_0 and plotted over the wavelength, $\lambda = 2\pi/k$. The *thick lines* represent the mean taken over 100 subsequent images in span- (*solid red*) and streamwise (*dashed black*) directions; *vertical lines* are placed at the positions of the peaks to guide the eye. *Re* is only accurate within ±10 for these runs. **a** $Re = 290$, **b** $Re = 340$, **c** $Re = 390$, **d** $Re = 440$

structures to a viscous scale. The wall shear stress, τ_w, required for the transformation was thereby obtained from a force balance at z_0 located toward the center of the channel:

$$\tau_w = \mu \frac{\partial u}{\partial z}\bigg|_{z_0} - \rho\langle u'w'\rangle, \tag{4}$$

where μ and ρ are the viscosity and the density of the fluid. Results for τ_w where normalized by τ_{w0}, the theoretical shear stress for a linear velocity profile, and are presented in Fig. 10. The normalized values are very close to unity throughout the laminar regime pointing to consistency and validating the method applied to determine τ_w. On the basis of this groundwork, it is possible to determine the viscous length given by $l^* = \nu/u_\tau$ where $u_\tau = \sqrt{\tau_w/\rho}$. It is remarkable that the equivalent of 100 viscous length scales, corresponding to the characteristic spacing of streaks in a boundary layer (Kline et al. 1967) and the optimum spanwise length scale reported by Waleffe (2003) for shear flows only coincides with the gap width at Reynolds numbers around $Re \approx 400$, close to the onset of the fully turbulent regime. Our observation further corroborates a conclusion drawn by Alfredsson and Matsubara (2000) stating that transition through instabilities of streaky structures and their consequent regeneration will only occur if $100l^*/d < 2$.

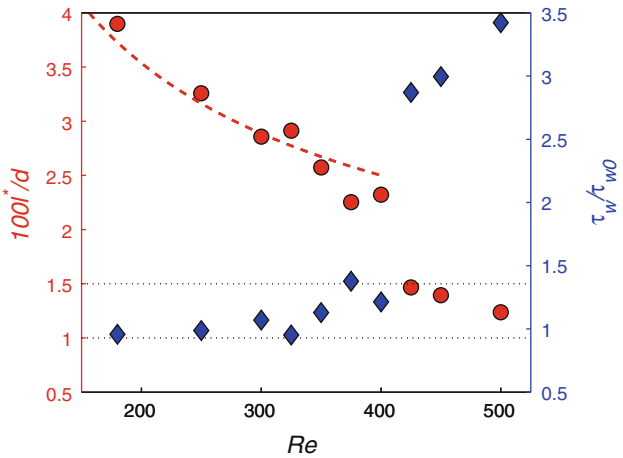

Fig. 10 Wall shear stress (*right axis*) normalized by the theoretical value in case of a linear velocity profile (*blue diamonds*) and $100l^*$ (*left axis*) as a function of the Reynolds number; measured (*red circles*) and calculated values for the linear velocity profile (*dashed line*). *Dotted horizontal lines* approximately indicate the range of observed vortex spacings (cf. Figs. 7, 9)

4 Numerical results

For comparison, we also performed numerical simulations on the range of Reynolds numbers from $Re = 370$ to $Re = 500$ (for details on the computation see Sect. 2) and

analyzed the data in terms of $\langle u'w' \rangle$ and TKE. It is known that turbulence in numerical cells may decay depending on initial conditions, the cell size, and the resolution (Hamilton et al. 1995; Schmiegel and Eckhardt 1997). Since our domain is not much larger than the minimum cell to sustain turbulence (Hamilton et al. 1995), no intermittent behavior can be expected. In our investigations, decay of turbulence was observed for some but not all Reynolds numbers below $Re = 415$. Whenever a decay occurred, it was sudden and quickly led to a completely laminar state. At the same time, the forcing via initial conditions was strong enough to trigger at least transient turbulence and none of the simulations ever exhibited a transitional regime as it was observed experimentally between $Re = 325$ and $Re = 400$. It therefore seemed appropriate to average numerical results only over periods of times in which the flow remained turbulent or, if this period was too short to obtain convergence on the turbulence statistics, to entirely discard runs that relaminarized. Hence, the presented numerical results inherently only characterize the turbulent regime.

Figure 11 presents a comparison between experimental and numerical results for $\langle u'w' \rangle$. In order not to overload the figure, only the values in the center of the channel (or the average over $0.45 < z < 0.55$ in case of the experiment), labeled $\langle u'w' \rangle_m$, are reported. It is obvious from the results that the simulations do not exhibit the same kind of transitional regime as the experiment. In fact, almost the same level of turbulence is reached at least for a transient for all Reynolds numbers investigated. The same observation can be made when looking at the comparison for the TKE data presented in Fig. 12. This figure also shows that the temporal fluctuations of the TKE in the simulations, represented in terms of their standard deviation by the shaded area, is of the order of the experimental scatter at a single Reynolds number. As Fig. 13 proves, the simulations also reproduce the distribution of the TKE into its single components very well. Probably, due to its confinedness, the wall-normal component in the turbulent regime remains about 3–4 times lower than the one associated with the spanwise direction in the simulation. This behavior is not as pronounced in the experimental data, which might be related to the fact that measurement noise is higher in the z-component. Quite interestingly, the streamwise component displays a rather consistent decrease with increasing Re, a feature that may also be present in the experimental data but remains less conclusive.

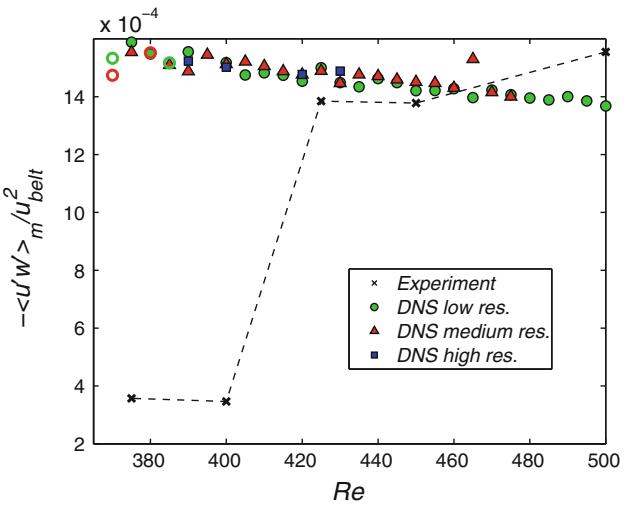

Fig. 11 Temporal and spatial averages of $\langle u'w' \rangle_m$ for simulations with different resolutions and the experiment. *Open symbols mark* runs in which the turbulence eventually decayed; in these cases, the mean was only taken over times in which the flow exhibited turbulence

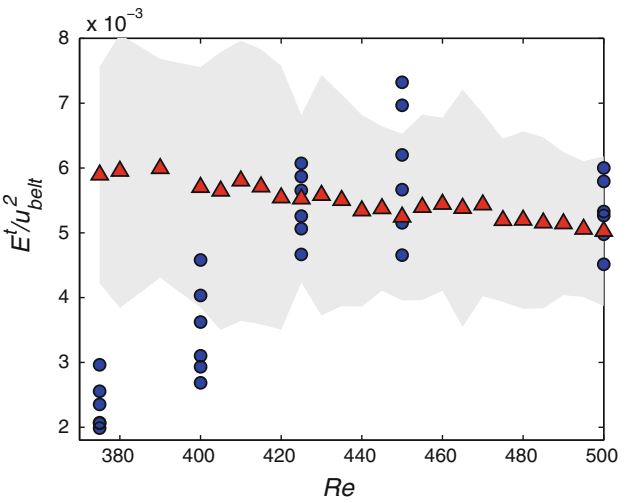

Fig. 12 Comparison of TKE results from experiment (*blue circles*) and simulation over turbulent periods (*red triangles*). The *shaded gray area* indicates the standard deviation of the temporal fluctuations of the numerically obtained values

5 Discussion

The transitional Reynolds number of $Re_{tr} = 370$ determined in this work agrees with the one found by Malerud et al. (1995). However, since transition largely depends on the specific perturbation that is for the most part unknown in our case, this number can merely serve as a means to judge the quality of our facility. For perturbations strong enough, it is shown that turbulence can be triggered at Reynolds numbers as low as $Re = 325$ (Bottin and Chaté 1998). From Figs. 5 and 11, we conclude that the inflow perturbations in our experiment do not suffice to trigger turbulence for $Re \leq 400$. This threshold is remarkably high in view of the fact that the perturbation at the inlet is expected to increase as the Reynolds number and thereby

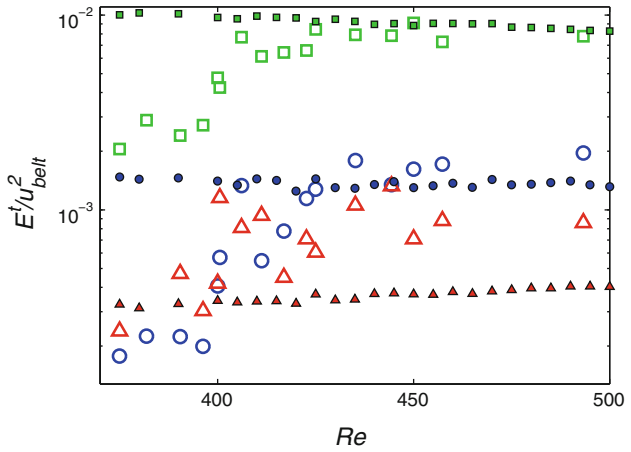

Fig. 13 Measured (*open symbols*, same data as in Fig. 5b) and calculated (*full symbols*) components of TKE ($\langle(u')^2\rangle$: *squares*, $\langle(v')^2\rangle$: *circles*, $\langle(w')^2\rangle$: *triangles*)

the pump setting as well as the mean dynamic pressure of the flow are increased. A fully turbulent regime on the level of the numerical predictions is only reached once Re exceeds 400, exactly the value at which Daviaud et al. (1992) report turbulence invading their flow domain. This observation is in strong support of a proposal by Prigent and Dauchot (2005) who suggests that the turbulent state becomes globally attractive at $Re = 400$ and only few initial conditions lead to a laminar flow for $Re > 400$. Within the turbulent regime, a very good agreement was found between experimental and numerical data validating our measurements. Combining Figs. 5 and 6, a transitional regime can be defined spanning from roughly $Re = 320$ to $Re = 400$. The lower value corresponds to the first significant increase in TKE, especially E^t_x, and $\langle u'w'\rangle$. The upper bound is not as well defined but chosen according to the jump in $\langle u'w'\rangle$ between $Re = 400$ and $Re = 425$. As mentioned earlier, this regime features no intermittency but is dominated by streamwise vortices that lead to intermediate values of $\langle u'w'\rangle$ and TKE. Its lower threshold coincides fairly well with the minimum Re of 325 at which sustained spots can be triggered (Bottin and Chaté 1998). While all of the measurements reported here were conducted increasing the Reynolds number possible hysteresis effects on the reverse transition were also investigated. In accordance with Malerud et al. (1995), no significant differences were found whether Re was decreased or increased before the measurements. All these observations are reminiscent of the regime of streamwise vortices observed by Bottin et al. (1998) when perturbing the flow by a spanwise wire. For very thin wires, they observed a transition to streamwise vortices at $Re = 305$ and turbulence for $Re > 370$ with no intermittent regime in between. It seems possible that the inflow profile behind the tapered honeycomb is susceptible to a similar kind of instability as the one triggered by the wire. However, an investigation into the linear stability of developing Couette profiles started from rest by Tillmark and Alfredsson (1992) revealed no growing modes. Another explanation is that in the sequence from noise to streaks and subsequent spot nucleation (Duguet et al. 2010), there is not enough time for secondary instabilities of the streaks to grow sufficiently and to cause their localized breakdown into turbulent spots. It remains an open topic to what extent the presented flow field lends itself to the study of such exciting features of pCf such as intermittent turbulence or oblique turbulent bands. The investigations so far could not answer this question conclusively. Apart from the flow field, there are some practical difficulties; namely these are the relatively short possible observation times due to the mean advection and the fact that transient changes of Re demand a simultaneous change of belt speed and pump setting that is hard to coordinate faithfully. The question will be subject of further studies.

So far, we were able to successfully establish a genuine pCf that is accessible to 3D-PTV. This enabled us to for the first time measure fully three-dimensional velocity fields resolving the entire gap width. In our study, we determined important quantities such as TKE and Reynolds shear stress. This goes along with a clear distinction of a laminar ($Re < 320$), a transitional ($320 < Re < 400$), and a fully turbulent regime ($Re > 400$). Lastly, we were able to characterize streamwise vortical structures that occurred mainly in the transitional regime in terms of 3D velocity fields and power spectra. A typical vortex spacing of roughly one gap width was observed. It could be shown that the onset of turbulence coincides with the Reynolds number at which $100l^*$, an optimum spanwise length scale in various shear flows (Kline et al. 1967; Waleffe 2003), roughly matches the gap width, i.e., transition occurs only when the outer scale exceeds the required inner scale.

Acknowledgments The first author would like to thank Lufthansa Technik AG for financial support during this study. The work was further kindly supported in part by the Swiss National Science Foundation under Grant number 2-77898-10.

References

Alfredsson PH, Matsubara M (2000) Free-stream turbulence, streaky structures and transition in boundary layer flows. AIAA Paper, pp 2000–2534

Antar G, Bottin S, Dauchot O, Daviaud F, Manneville P (2003) Details on the intermittent transition to turbulence of a locally forced plane Couette flow. Exp Fluids 34:324–331. doi:10.1007/s00348-002-0560-2

Aydin EM, Leutheusser HJ (1991) Plane-Couette flow between smooth and rough walls. Exp Fluids 11:302–312. doi:10.1007/BF00194862

Barkley D, Tuckerman LS (1999) Stability analysis of perturbed plane Couette flow. Phys Fluids 11(5):1187–1195. doi:10.1063/1.869987

Barkley D, Tuckerman LS (2007) Mean flow of turbulent-laminar patterns in plane Couette flow. J Fluid Mech 576:109–137. doi:10.1017/S002211200600454X

Bech KH, Tillmark N, Alfredsson PH, Andersson HI (1995) An investigation of turbulent plane Couette flow at low Reynolds numbers. J Fluid Mech 286:291–325. doi:10.1017/S0022112095000747

Bottin S, Chaté H (1998) Statistical analysis of the transition to turbulence in plane Couette flow. Eur Phys J B 6(1):143–155. doi:10.1007/s100510050536

Bottin S, Dauchot O, Daviaud F (1997) Intermittency in a locally forced plane Couette flow. Phys Rev Lett 79(22):4377–4380. doi:10.1103/PhysRevLett.79.4377

Bottin S, Dauchot O, Daviaud F, Manneville P (1998) Experimental evidence of streamwise vortices as finite amplitude solutions in transitional plane Couette flow. Phys Fluids 10(10):2597–2607. doi:10.1063/1.869773

Canuto C, Hussaini M, Quarteroni A, Zang T (1998) Spectral methods in fluid dynamics. Springer, Berlin

Dauchot O, Daviaud F (1995) Streamwise vortices in plane Couette flow. Phys Fluids 7(5):901–903. doi:10.1063/1.868565

Daviaud F, Hegseth J, Bergé P (1992) Subcritical transition to turbulence in plane Couette flow. Phys Rev Lett 69(17):2511–2514. doi:10.1103/PhysRevLett.69.2511

Duguet Y, Schlatter P, Henningson DS (2010) Formation of turbulent patterns near the onset of transition in plane Couette flow. J Fluid Mech 650:119–129. doi:10.1017/S0022112010000297

Gibson JF (2009) Channelflow Users' Manual. 0.9.18 edn, URL http://www.channelflow.org

Gibson JF, Halcrow J, Cvitanović P (2008) Visualizing the geometry of state space in plane Couette flow. J Fluid Mech 611:107–130

Gibson JF, Halcrow J, Cvitanović P (2009) Equilibrium and travelling-wave solutions of plane Couette flow. J Fluid Mech 638:243–266. doi:10.1017/S0022112009990863

Hamilton JM, Kim J, Waleffe F (1995) Regeneration mechanisms of near-wall turbulence structures. J Fluid Mech 287:317–348. doi:10.1017/S0022112095000978

Hegseth JJ (1996) Turbulent spots in plane Couette flow. Phys Rev E 54(5):4915–4923. doi:10.1103/PhysRevE.54.4915

Kline SJ, Reynolds WC, Schraub FA, Runstadler PW (1967) The structure of turbulent boundary layers. J Fluid Mech 30(04):741–773. doi:10.1017/S0022112067001740

Maas HG, Gruen A, Papantoniou D (1993) Particle tracking velocimetry in three-dimensional flows. Exp Fluids 15:133–146. doi:10.1007/BF00190953

Malerud S, Måløy KJ, Goldburg WI (1995) Measurements of turbulent velocity fluctuations in a planar Couette cell. Phys Fluids 7(8):1949–1955. doi:10.1063/1.868509

Malik NA, Dracos T, Papantoniou DA (1993) Particle tracking velocimetry in three-dimensional flows. Exp Fluids 15:279–294. doi:10.1007/BF00223406

Matisse P, Gorman M (1984) Neutrally buoyant anisotropic particles for flow visualization. Phys Fluids 27(4):759–760. doi:10.1063/1.864702

Nagata M (1990) Three-dimensional finite-amplitude solutions in plane Couette flow: bifurcation from infinity. J Fluid Mech 217:519–527. doi:10.1017/S0022112090000829

Nagata M (1997) Three-dimensional traveling-wave solutions in plane Couette flow. Phys Rev E 55(2):2023–2025. doi:10.1103/PhysRevE.55.2023

Ouellette N, Xu H, Bodenschatz E (2006) A quantitative study of three-dimensional lagrangian particle tracking algorithms. Exp Fluids 40:301–313. doi:10.1007/s00348-005-0068-7

Peyret R (2002) Spectral methods for incompressible flows. Springer, Berlin

Philip J, Manneville P (2011) From temporal to spatiotemporal dynamics in transitional plane Couette flow. Phys Rev E 83(3):036308. doi:10.1103/PhysRevE.83.036308

Prigent A, Dauchot O (2005) Transition to versus from turbulence in subcritical couette flows. In: Madylam RM, Mullin T, Kerswell R (eds) IUTAM symposium on laminar-turbulent transition and finite amplitude solutions, fluid mechanics and its applications, Springer, Netherlands, pp 195–219. doi:10.1007/1-4020-4049-0_11

Prigent A, Grgoire G, Chat H, Dauchot O (2003) Long-wavelength modulation of turbulent shear flows. Physica D 174(1–4):100–113. doi:10.1016/S0167-2789(02)00685-1

Racca RG, Dewey JM (1988) A method for automatic particle tracking in a three-dimensional flow field. Exp Fluids 6:25–32. doi:10.1007/BF00226131

Reichardt H (1959) Über die Geschwindigkeitsverteilung in einer geradlinigen turbulenten Couette Strömung. Mitteilung aus dem Max-Planck-Institut für Strömungsforschung Nr. 22

Rolland J, Manneville P (2011) Pattern fluctuations in transitional plane Couette flow. J Stat Phys 142:577–591. doi:10.1007/s10955-011-0126-x

Schmiegel A, Eckhardt B (1997) Fractal stability border in plane couette flow. Phys Rev Lett 79(26):5250–5253. doi:10.1103/PhysRevLett.79.5250

Schmiegel A, Eckhardt B (2000) Persistent turbulence in annealed plane Couette flow. Europhys Lett 51(4):395–400. doi:10.1209/epl/i2000-00507-2

Schneider TM, Marinc D, Eckhardt B (2010) Localized edge states nucleate turbulence in extended plane couette cells. J Fluid Mech 646:441–451. doi:10.1017/S0022112009993144

Tennekes H, Lumley J (1994) A first course in turbulence. MIT Press, Cambridge, MA

Tillmark N, Alfredsson PH (1992) Experiments on transition in plane Couette flow. J Fluid Mech 235:89–102. doi:10.1017/S0022112092001046

Tuckerman LS, Barkley D (2011) Patterns and dynamics in transitional plane Couette flow. Phys Fluids 23(4):041301. doi:10.1063/1.3580263

Virant M, Dracos T (1997) 3d ptv and its application on lagrangian motion. Meas Sci Technol 8(12):1539. doi:10.1088/0957-0233/8/12/017

Waleffe F (1997) On a self-sustaining process in shear flows. Phys Fluids 9(4):883–900. doi:10.1063/1.869185

Waleffe F (2003) Homotopy of exact coherent structures in plane shear flows. Phys Fluids 15(6):1517–1534. doi:10.1063/1.1566753